ACTA METALLURGICA SLOVACA
2023, VOL. 29, NO. 4, 210-213

RESEARCH PAPER

# INFLUENCE OF SINTERING TEMPERATURE ON THE STRUCTURAL OF $Mg_2Si_{0.3}Sn_{0.7}$ ALLOY PREPARED BY POWDER METALLURGY

*I Nyoman Gede Putrayasa Astawa[1], Muhammad Yunan Hasbi[1], Septian Adi Chandra[1], Dedi Pria Utama[1], Rahadian Roberto[1], Agung Imaduddin[2], Sigit Dwi Yudanto[1]*

1 Research Center for Metallurgy, National Research and Innovation Agency, Gedung 720, KST BJ Habibie, Serpong, Tangerang Selatan, Banten, 15314, Indonesia
2 Research Center for Advanced Materials, National Research and Innovation Agency, Gedung 720, KST BJ Habibie, Serpong, Tangerang Selatan, Banten, 15314, Indonesia

*Corresponding author: sigi012@brin.go.id, tel.: +6281213024663, Research Center for Metallurgy, National Research and Innovation Agency, Gedung 720, KST BJ Habibie, Serpong, Tangerang Selatan, Banten, 15314, Indonesia

Received: 04.10.2023
Accepted: 22.11.2023

## ABSTRACT

The efficiency of energy consumption can be improved by reducing the heat lost during the combustion process of automotive engines. By converting waste heat energy into other energy sources that can be used directly, efficiency can be achieved. $Mg_2Si_{0.3}Sn_{0.7}$ is a metal alloy that has the potential to convert waste heat into power. In this research, we used the powder metallurgy method to synthesize the $Mg_2Si_{0.3}Sn_{0.7}$-based alloy. A mixture of Mg, Si, and Sn powders that had been milled for 2 hours was insulated in the stainless-steel tube to avoid oxidation and combustion. Heat treatment was conducted with temperature variations of 700, 750, and 800°C for 4 hours to investigate the influence of sintering temperature on the crystal structure of the $Mg_2Si_{0.3}Sn_{0.7}$-based alloy. The microstructure and formation of the material were examined using an X-ray diffractometer (XRD) and a scanning electron microscope (SEM). Based on XRD analysis, it was found that the $Mg_2Si_{0.3}Sn_{0.7}$ phase and a small amount of magnesium oxide (MgO) phase have formed. Due to the phase transition from $Mg_2Si_{0.3}Sn_{0.7}$ to $Mg_2Sn$ at a sintering temperature of 800°C, the cubic lattice constant ***-a*** changes from 0.6631 nm to 0.6765 nm.

**Keywords:** waste heat; Mg2Si0.3Sn0.7; metal alloy; crystal structure; phase transition

## INTRODUCTION

Fossil fuels as a fuel in various fields such as transportation, electricity generation and industry are still an option today. In general, the majority of processes generate a substantial amount of waste heat. The use of wasted thermal energy can lead to an increase in fuel consumption. Through the Seebeck and Peltier phenomena, this heat can be converted directly into other energy sources. The Seebeck phenomenon states that if two materials have a temperature difference between their surfaces, a potential difference will result in both materials. Furthermore, this material will be known as a thermoelectric material. When a material has a potential difference, the Peltier phenomenon states that applying heat to one surface will result in a cool temperature on the opposite surface. This material is referred to as a thermocooler material.

Magnesium based metal alloys, such as Mg2Si, Mg2Ge, and Mg2Sn, have the potential to be used as thermoelectric materials. The ZT value of a material can be used to determine its thermoelectricity (ZT>1) The ZT values for the three magnesium-based alloys are still lower than 1. Enhancing thermoelectric properties, particularly the ZT value, has been achieved through doping in materials. When Sn and Ge elements are doped on the Si site, the ZT value of Mg2Si-based alloys increases [1]. The Mg2Si0.3Sn0.7 alloy has thermoelectric properties that are similar to those of p-type thermoelectric materials [1]–[4]. The ZT value of the Mg2Si0.3Sn0.7-based alloy was increased up to 1.4 by doping several elements [1].

The Mg2Si0.3Sn0.7 alloy generation process is generally based on the phase diagram of the Mg-Si-Sn system or pseudo-binary Mg2Si-Mg2Sn [5]–[7]. When manufacturing the Mg2Si0.3Sn0.7-based alloy, the heating method is challenging. Kun Cheng et al synthesized the Mg2Si0.3Sn0.7-based alloy through the melting technique [2]. Magnesium, silicon, and tin were weighed in accordance with their respective stoichiometric compositions of Mg2.03Si0.3Sn0.7 and then all of the components were sealed in a tantalum tube. The melting occurred at 1057°C for 7 hours, was quenched in water, and then annealed for 72 hours at 700°C. Huang et al employed the solid-state reaction approach followed by hot pressing to synthesize the Mg2(Si0.3Sn0.7)0.99Sb0.01 alloy [8]. After the raw materials Mg, Si, Sn, and Sb have been weighed in accordance with the formula, they are mixed and put on a Mo crucible. To prevent the formation of magnesium oxide, the sample was carefully sealed in a silica tube before the heating procedure. At 580°C, the sample was heated for 15 hours at a relatively low heat rate. The heat-treated products are crushed and then heated to 750°, 800°, and a combination of the two temperatures during a hot-pressing process. The solid-state reaction method led to the formation of Mg2Si0.3Sn0.7, Mg2Si, and Mg2Sn phases based on their X-ray diffraction investigation. When it was combined with hot pressing, the method was found to be effective in producing Mg2Si0.3Sn0.7-based alloy.

In this study, we report that the sintering temperature influences the evolution from the Mg2Si0.3Sn0.7 phase to the Mg2Sn

phase. Through X-ray diffraction and scanning electron microscope investigations, it was discovered that the growth of grains occurred with an increase in sintering temperatures.

## MATERIAL AND METHODS

### Sample preparation

Powder metallurgy was employed to synthesize the $Mg_2Si_{0.3}Sn_{0.7}$-based alloy using commercially available magnesium powders (Merck Millipore), silicon powders (Sigma Aldrich), and tin powders (Sigma Aldrich) as initial materials. To prepare the $Mg_2Si_{0.3}Sn_{0.7}$- based alloy, Mg, Si and Sn powders were weighed at the atomic ratio of Mg:Si:Sn=2:0.3:0.7. The initial powders were then ground for 2 hours in a shaker mill to further homogenize the mixture. In the milling process, steel balls are employed at a ratio of ball to powders weight (BPR) of 2:1. The milled powder is sealed and compacted in a stainless-steel tube. This technique has been demonstrated to be effective in minimizing magnesium oxidation while sintering process at high temperatures (above the melting point of Mg) [9], [10]. The samples were then sintered in a muffle furnace with variations in temperature of 700, 750 and 800°C for 4 hours. After the holding time was reached, all samples were permitted to naturally cool to room temperature in the furnace. The samples in this research were coded and presented in **Table 1**. To characterize the sintered samples, it was divided into two sections. For X-ray diffraction (XRD) testing, a piece was mechanically removed from the stainless-steel tube and ground using agate mortar. To observe the morphology of the surface samples, the other pieces are inserted into the resin to be grinded and polished.

### Sample characterization

In this study, we investigate the phase formed after the sintering process using an XRD. The testing was conducted at room temperature with a step size of 0.01° and an angle range of 2θ = 20-80°. The Rigaku Smart Lab X-ray diffractometer, which has a 240 mm goniometer radius, is operated by a copper radiation source (Cu kα = 0.15406 nm). Qualitative and quantitative characterization was carried out to investigate the effect of sintering temperature on the phase and its crystal structure. The Rietveld method is employed to determine the lattice parameters of the phase that was obtained [11]. The surface morphology of the samples was observed using a JEOL JSM6390A scanning electron microscope (SEM). The sample surface that observed was a sintered solid surface that had been grinded and polished. The distribution of elements on the sample surface was determined through element mapping - energy dispersive X-ray spectroscopy (Mapping-EDAXS).

**Table 1** $Mg_2Si_{0.3}Sn_{0.7}$-based alloy samples code with heat treatment variation.

| Sample code | Milling time (hours) | T-sintering (°C) | Holding time (hours) |
|---|---|---|---|
| M700 | 2 | 700 | 4 |
| M750 | 2 | 750 | 4 |
| M800 | 2 | 800 | 4 |

## RESULTS AND DISCUSSION

Following 4 hours of sintering at 700, 750, and 800°C, **Fig. 1** shows the powder X-ray diffraction (PXRD) patterns of $Mg_2Si_{0.3}Sn_{0.7}$-based alloy samples. The diffraction pattern for samples sintered at temperatures of 700 and 750°C shows peaks at angles of 2θ = 23.25, 26.74, 38.25, 45.19, 55.07, 60.64, 68.93, and 73.79°. Similar diffraction peaks may be seen at this angle in the planes indexed (111), (200), (220), (311), (400), (311), (422), and (511), which are the planes of the cubic phase $Mg_2Si_{0.3}Sn_{0.7}$ [4], [12]–[15]. There is a peak that matches the MgO phase peak at angles 2θ = 42.90 and 62.30° [14]. These findings demonstrate that, despite sintering temperatures over the Mg melting point, the method employed can maintain the $Mg_2Si_{0.3}Sn_{0.7}$ phase formation with less MgO. The $SiO_2$ phase was detected at an angle of 2θ = 20.89°. The presence of the $SiO_2$ is a follow-up impurity phase from the silicon powder raw material used [16]. In comparison to M700 and M750, the sample sintered at 800°C (M800) has a significant difference. The diffraction peaks have been shifted to the left. Based on the investigation results, the peaks were detected at angles 2θ = 22.77, 26.36, 37.61, 44.41, 46.49, 54.21, 59.54, 67.83, and 72.56°. According to Boudemagh et al and Huang et al, these peaks are correspond to the cubic $Mg_2Sn$ phase [8], [17]. On sintering at a temperature of 800°C it turns out to give rise to a cubic phase of $Mg_2Si$ which is detected at an angle of 2θ = 23.95°. The occurrence of the $Mg_2Si$ phase is most likely due to sintering temperatures exceeding the melting point of the $Mg_2Si_{0.3}Sn_{0.7}$ alloy, causing the $Mg_2Si_{0.3}Sn_{0.7}$ phase to decompose into $Mg_2Sn$ and $Mg_2Si$ [18]. The $Mg_2Sn$ alloy melts at a temperature of 774 °C [5], [6].

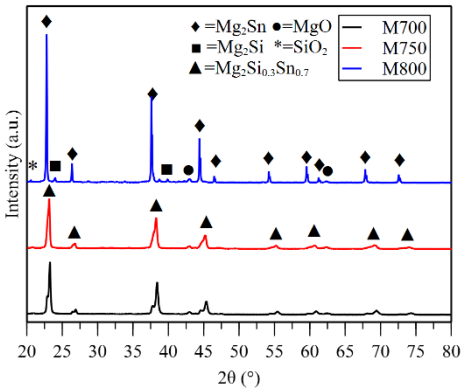


**Fig. 1** Powder X-ray diffraction (PXRD) pattern of $Mg_2Si_{0.3}Sn_{0.7}$-based alloy samples.

**Fig. 2a** illustrates the shift in the diffraction peak of the $Mg_2Si_{0.3}Sn_{0.7}$-based alloy sample when the diffraction pattern is enlarged in the angle range 2θ = 22.2–23.8°. The pattern indicates that the highest peak of the $Mg_2Si_{0.3}Sn_{0.7}$ sample has been moved by 0.48°. A peak shift and a phase transition from $Mg_2Si_{0.3}Sn_{0.7}$ to $Mg_2Sn$ occur when the sintering temperature increases. Between the $Mg_2Si_{0.3}Sn_{0.7}$ and the $Mg_2Sn$ phase, an intermediate arises. Additionally, Mejri et al reported the existence of this intermediary phase [6].

According to **Fig. 2a**, a higher sintering temperature results in a more crystallin phase of $Mg_2Si_{0.3}Sn_{0.7}$-based alloy. This indicates that the phase peak intensity value has increased by up to three times. According to the phase diagram of the Mg-Si-Sn system, the sintering process has reached the melting point of the $Mg_2Si_{0.3}Sn_{0.7}$ phase, which has led to a rise in crystallinity. As a result, phase formation now occurs through a solidification mechanism, instead of continuing as a liquid solid process.

The Monshi-Scherrer method was utilized to determine the size of the crystallite to determine the impact of sintering temperature on the microstructure [19], [20]. A linear line equation can be created using the ln (1/cos θ) vs ln FWHM plot, as displayed

in **Fig. 2b**. The full width at half maximum (FWHM) of the three samples in the indexed planes (111), (220), (311), and (331), expressed in degrees, are shown in **Table 2**. After that, the crystal size is determined using this FWHM value. Line equations M700, M750, and M800 samples have constant **c** values of -5.5640, -5.8441, and -6.6683, respectively. As the sintering temperature rises, crystals of the $Mg_2Si_{0.3}Sn_{0.7}$-based alloy grow, as presented in **Table 2**.

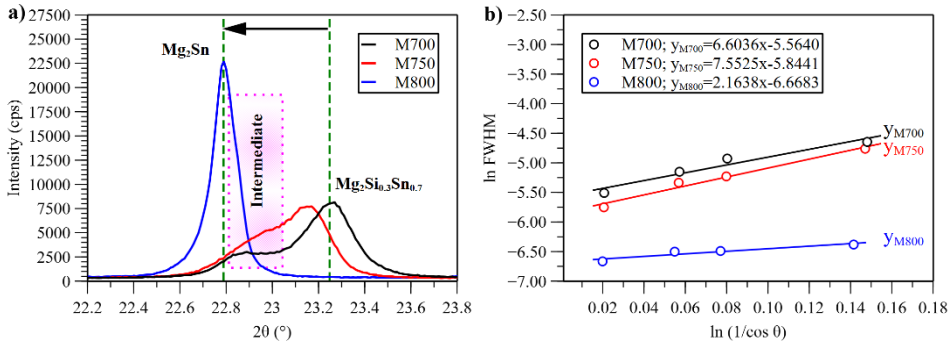


**Fig. 2** Peak shift results from magnification of the diffraction pattern at 22.2 – 23.8° on the $Mg_2Si_{0.3}Sn_{0.7}$-based alloy samples (a) and Plot of ln (1/cos θ) vs ln FWHM of $Mg_2Si_{0.3}Sn_{0.7}$-based alloy samples.

**Table 2** Quantitative analysis of $Mg_2Si_{0.3}Sn_{0.7}$-based alloy samples.

| Source | M700 | M750 | M800 |
|---|---|---|---|
| Lattice constants -***a*** (nm) | 0.6631 | 0.6670 | 0.6765 |
| FWHM (111) (°) | 0.232 | 0.182 | 0.073 |
| FWHM (220) (°) | 0.332 | 0.276 | 0.086 |
| FWHM (311) (°) | 0.415 | 0.307 | 0.087 |
| FWHM (331) (°) | 0.550 | 0.490 | 0.097 |
| Crystallite size (nm) | 38 | 50 | 114 |

**Fig. 3** shows the refinement of the diffraction pattern of the $Mg_2Si_{0.3}Sn_{0.7}$-based alloy sample sintered at 800°C. $Mg_2Sn$, $Mg_2Si$, MgO, and $SiO_2$ were the 4 phases used in the refinement process that were detected qualitatively. The $Mg_2Sn$ phase input for the calculation process is modified by using the $Mg_2Si_{0.3}Sn_{0.7}$ formula and a cubic structure that is part of the space group fm-3m [7]. The lattice constant ***-a*** at 0.6765 nm, as calculated, is similar to the lattice constant value of the $Mg_2Sn$ phase reported by Boudemagh et al [17]. The lattice constant ***-a*** for all $Mg_2Si_{0.3}Sn_{0.7}$-based alloy samples are tabulated in **Table 2**. Despite calculations using the modified $Mg_2Sn$ phase, the lattice constants values of the M800 sample remained close to the $Mg_2Sn$ lattice constants value. This is in contrast to the M700 and M750 samples, which have the lattice constants ***-a*** value of 0.6631 nm and 0.6670 nm, respectively. According to Goyal et al, the $Mg_2Si_{0.3}Sn_{0.7}$-based alloy synthesized by the melting technique has the lattice constants ***-a*** of 0.6655 nm [3]. $Mg_2Si_{0.3}Sn_{0.7}$-based alloy was synthesized by Assahsahi et al through melting and spark plasma sintering (SPS) [4]. They provided information on the lattice constants ***-a*** value of the $Mg_2Si_{0.3}Sn_{0.7}$ phase at 0.6660 nm [4]. These findings indicate that the phase transition of $Mg_2Si_{0.3}Sn_{0.7}$ phase is influenced by the sintering temperature. The $Mg_2Si_{0.3}Sn_{0.7}$ alloy will tend to turn into $Mg_2Sn$ alloy when heated above its melting point of $Mg_2Sn$.

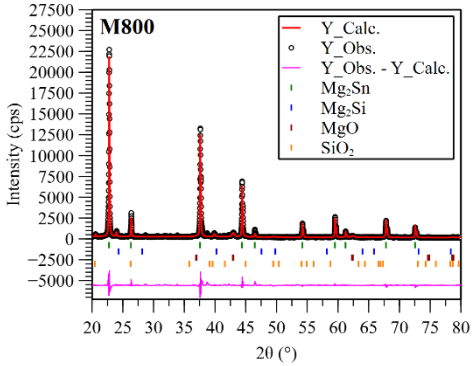


**Fig. 3** Refined pattern of the sample sintered at 800°C.

**Fig. 4a** – **4c** are surface images of $Mg_2Si_{0.3}Sn_{0.7}$-based alloy samples after grinding and polishing processes. **Fig. 4a** shows the polishing surface of the M700 sample with irregular shapes and random directions. There are no significant metallic grain connections evident in the surface morphology of the M700 sample. As the sintering temperature increases, the surface begins to have a direction marked by polishing traces. The sample was sintered at 750°C and its surface microstructure is shown in **Fig. 4b**. It appears that a metallic morphology has begun to form with a regular shape compared to the sample sintered at 700°C. **Fig. 4c** demonstrates the polished surface with an enlarging grain surface. This is supported by the XRD analysis in **Table 2** which shows that crystal growth occurs with increasing sintering temperature. In addition, the metal surface shows the majority of $Mg_2Sn$ phase present in the M800 sample.

**Fig. 5a** and **5b** show the distribution of the elements contained on the surface of the $Mg_2Si_{0.3}Sn_{0.7}$-based alloy sample sintered at 700 and 750°C. The elements mapping image indicates that magnesium and tin elements are the dominant elements throughout the observation area. The alloy formula was created based on the content of these two elements, which is the reason for this. Magnesium oxide (MgO) is the most likely substance in **Fig. 5b**, which is marked with a red line. It can be seen that the area with

the red line has a distribution that is dominated by magnesium and oxygen.

The mapping results (**Fig. 5a - 5b**) show that the sample elements M700 and M750 have the same distribution of elemental oxygen (O) with low intensity. The XRD results of the two samples validate this, indicating that the MgO produced is quite low.

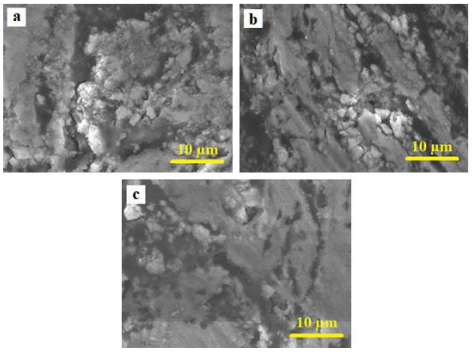


**Fig. 4**. Surface images of the $Mg_2Si_{0.3}Sn_{0.7}$-based alloy samples. a) M700 sample, b) M750 sample, and c) M800 sample

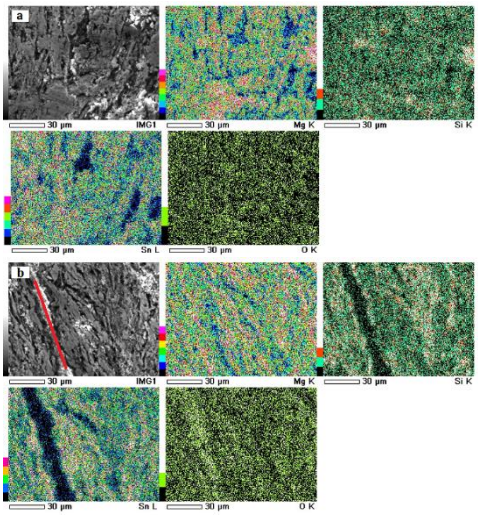


**Fig. 5** SEM-EDAXS mapping of M700 sample (a) and M750 sample (b).

## CONCLUSIONS

$Mg_2Si_{0.3}Sn_{0.7}$-based alloy has successfully been synthesized using the powder metallurgy method. An X-ray diffractometer (XRD) and a scanning electron microscope (SEM) were used to investigate synthesized samples with variations in sintering temperature. Following is a list of some findings from the present research:

1. The alloying process is maintained successfully with minor magnesium oxide by heating in the stainless-steel tube.
2. The cubic $Mg_2Si_{0.3}Sn_{0.7}$ phase is formed when sintering at temperatures below 800°C.
3. The cubic $Mg_2Si_{0.3}Sn_{0.7}$ phase is turned into the cubic $Mg_2Sn$ phase by the sintering process at 800°C. Evidence for this phenomenon can be found in the lattice constants - ***a***, which have a value change from 0.6631 nm to 0.6765 nm.
4. As the sintering temperature increases, the surface of the $Mg_2Si_{0.3}Sn_{0.7}$-based alloy becomes clearer, which leads to grain growth.

**Acknowledgments:** This contribution was created under the support of the project Rumah Program Material Maju - Organisasi Riset Nanoteknologi dan Material, National Research and Innovation Agency with contract number 6/III.10.2/HK/2023. The authors acknowledge the facilities, scientific and technical support from Materials and Metallurgical Characterization Laboratories and Advanced Characterization Laboratories Serpong, National Research and Innovation Agency through E-Layanan Sains, Badan Riset dan Inovasi Nasional (BRIN).

## REFERENCES

1. R. Santos, S. Aminorroaya Yamini, S. X. Dou: Journal of Materials Chemistry A, 6 (8), 2018, 3328–3341. https://doi.org/10.1039/c7ta10415d.
2. K. Cheng, Z. Bu, J. Tang, X. Zhang, X. Meng, W. Li: Materials Today Physics, 28, 2022, 100887. https://doi.org/10.1016/j.mtphys.2022.100887.
3. G. K. Goyal, S. Mukherjee, R. C. Mallik, S. Vitta, I. Samajdar, T. Dasgupta: ACS Applied Energy Materials, 2, 2019, 2129−2137. https://doi.org/10.1021/acsaem.8b02148.
4. I. Assahsahi, B. Popescu, R. El Bouayadi, D. Zejli, M. Enculescu, A. Galatanu: Journal of Alloys and Compounds, 944, 2023, 169270. https://doi.org/10.1016/j.jallcom.2023.169270.
5. I. Jung, D. Kang, W. Park, N. J. Kim, S. Ahn: Computer Coupling of Phase Diagrams and Thermochemistry, 31, pp. 192–200, 2007. http://doi.org/10.1016/j.calphad.2006.12.003.
6. A. Kozlov, J. Gröbner, R. Schmid-Fetzer: Journal of Alloys and Compounds, 509, 2011, 3326–3337. https://doi.org/10.1016/j.jallcom.2010.12.052.
7. K. Yin, Q. Zhang, Y. Zheng, X. Su, X. Tang, C. Uher: Journal of Materials Chemistry C, 3, 2015, 10381–10387. https://doi.org/10.1039/C5TC01434D.
8. H. Huang, P. Wen,S. Deng, X. Zhou, B. Duan, Y. Li, P. Zhai: Journal of Alloys and Compounds, 881, 2021, 160546. https://doi.org/10.1016/j.jallcom.2021.160546.
9. M. Y. Hasbi, S. A. Chandra, A. Fitriani, L. Suhaimi, S. D. Yudanto, Science of Sintering, 55, 2023, 81–88. https://doi.org/10.2298/SOS2301081Y.
10. S. D. Yudanto, Y. P. Dewi, P. Sebayang, S. A. Chandra, A. Imaduddin, B. Kurniawan, A. Manaf: Journal of Metals, Materials and Minerals, 30, 2020, 9–14. https://doi.org/ 10.14456/jmmm.2020.32.
11. A. C. Larson, R. B. Von Dreele: *Los Alamos National Laboratory Report LAUR 86-748*, 748. 2004.
12. H. Kamila, A. Sankhla, M. Yasseri, N. P. Hoang, N. Farahi: Materials Today: Proceedings, 8, 2019, 546–555. https://doi.org/10.1016/j.matpr.2019.02.052.
13. G. Castillo-hernandez, M. Yasseri, B. Klobes, S. Ayachi, E. Müller, J. De Boor: Journal of Alloys and Compounds, 845, 2020, 156205. https://doi.org/10.1016/j.jallcom.2020.156205.
14. M. Yasseri, A. Sankhla, H. Kamila, R. Orenstein: Acta Materialia, 185, 2020, 80–88. https://doi.org/10.1016/j.actamat.2019.11.054.
15. Q. Zhang, Y. Zheng, X. Su, K. Yin, C. Uher: Scripta Materialia, 96, 2015, 1–4. https://doi.org/10.1016/j.scriptamat.2014.09.009.
16. S. A. Chandra, R. Roberto, D. P. Utama, D. Zulkarnain, D. S. P. Bratawan, M. S. Suherman, A. Gayatri, A. Tjahjono, M. Y. Hasbi, S. D. Yudanto: Acta Metallurgica Slovaca, 29, 2023, 108–112. https://doi.org/10.36547/ams.29.2.1840.
17. D. Boudemagh, D. Fruchart, R. Haettel, E.K. Hlil, A. Lacoste, L. Ortega, N. Skryabina, J. Tobola, P. Wolfers: Solid State Phenomena, 170, 2011, 253–258. https://doi.org/10.4028/www.scientific.net/SSP.170.253.
18. H. Inoue, M. Kato, I. J. Ohsugi: Transactions of the Materials Research Society of Japan, 39 (2), 2014, 221-223. https://doi.org/10.14723/tmrsj.39.221.
19. S. D. Yudanto, S. A. Chandra, R. Roberto, D. P. Utama, V. O. Herlina, Lusiana: Journal of Ceramic Processing Research, 23 (3), 2022, 287–291. https://doi.org/10.31857/s0044457x22020076.
20. A. Monshi, M. R. Foroughi, M. R. Monshi: World Journal of Nano Science and Engineering, 2, 2012, 154–160. http://doi.org/10.4236/wjnse.2012.23020.